tvst

Retina

Focused Ultrasound as a Novel Non-Invasive Method for the Delivery of Gold Nanoparticles to Retinal Ganglion Cells

Younghoon Park[1], Jaewoo Shin[2–4], Junwon Park[5], Seulbi Kim[6], Ji Hun Park[6], Jaeheung Kim[7], Chang Seok Kim[7], Jin Woo Chang[5], Carol Schuurmans[3,4,8], Isabelle Aubert[3,4], Won Seok Chang[5], and Kyungsik Eom[1]

[1] Department of Electronics Engineering, College of Engineering, Pusan National University, Busan, Republic of Korea
[2] Medical Device Development Center, Daegu-Gyeongbuk Medical Innovation Foundation (K-MEDI Hub), Daegu, Republic of Korea
[3] Biological Sciences, Hurvitz Brain Sciences Research Program, Sunnybrook Research Institute, Toronto, Ontario, Canada
[4] Department of Laboratory Medicine and Pathobiology, University of Toronto, Toronto, Ontario, Canada
[5] Department of Neurosurgery, Brain Research Institute, Yonsei University College of Medicine, Seoul, Republic of Korea
[6] Department of Science Education, Ewha Womans University, Seoul, Republic of Korea
[7] Department of Cogno-Mechatronics Engineering, Pusan National University, Busan, Republic of Korea
[8] Department of Biochemistry, University of Toronto, Toronto, Ontario, Canada

Correspondence: Isabelle Aubert, Department of Laboratory Medicine and Pathobiology, University of Toronto, 2075 Bayview Ave., Toronto, ON M4N 3M5, Canada. e-mail: isabelle.aubert@utoronto.ca
Won Seok Chang, Department of Neurosurgery, Brain Research Institute, Yonsei University College of Medicine, 50-1, Yonsei-Ro, Seodaemun-gu, Seoul 03722, Republic of Korea. e-mail: changws0716@yuhs.ac
Kyungsik Eom, Department of Electronics Engineering, College of Engineering, Pusan National University, 2, Busandaehak-ro 63beon-gil, Geumjeong-gu, Busan 46241, Republic of Korea. e-mail: kseom@pusan.ac.kr

Received: August 17, 2023
Accepted: February 22, 2024
Published: May 7, 2024

Keywords: blood–retinal barrier; drug delivery; gold nanoparticles; focused ultrasound; label-free imaging

Citation: Park Y, Shin J, Park J, Kim S, Park JH, Kim J, Kim CS, Chang JW, Schuurmans C, Aubert I, Chang WS, Eom K. Focused ultrasound as a novel non-invasive method for the delivery of gold nanoparticles to retinal ganglion cells. Transl Vis Sci Technol. 2024;13(5):5, https://doi.org/10.1167/tvst.13.5.5

Purpose: The blood–retinal barrier (BRB) restricts the delivery of intravenous therapeutics to the retina, necessitating innovative approaches for treating retinal disorders. This study sought to explore the potential of focused ultrasound (FUS) to non-invasively deliver intravenously administered gold nanoparticles (AuNPs) across the BRB. FUS–BRB modulation can offer a novel method for targeted retinal therapy.

Methods: AuNPs of different sizes and shapes were characterized, and FUS parameters were optimized to permeate the BRB without causing retinal damage in a rodent model. The delivery of 70-kDa dextran and AuNPs to the retinal ganglion cell (RGC) layer was visualized using confocal and two-photon microscopy, respectively. Histological and statistical analyses were conducted to assess the effectiveness and safety of the procedure.

Results: FUS–BRB modulation resulted in the delivery of dextran and AuNPs to the RGC and inner nuclear layer. Smaller AuNPs reached the retinal layers to a greater extent than larger ones. The delivery of dextran and AuNPs across the BRB with FUS was achieved without significant retinal damage.

Conclusions: This investigation provides the first evidence, to our knowledge, of FUS-mediated AuNP delivery across the BRB, establishing a foundation for a targeted and non-invasive approach to retinal treatment. The results contribute to developing promising non-invasive therapeutic strategies in ophthalmology to treat retinal diseases.

Translational Relevance: Modifying the BRB with ultrasound offers a targeted and non-invasive delivery strategy of intravenous therapeutics to the retina.

translational vision science & technology

Copyright 2024 The Authors

Downloaded from tvst.arvojournals.org on 11/11/2024
This work is licensed under a Creative Commons Attribution-NonCommercial-NoDerivatives 4.0 International License.

Introduction

Gold nanoparticles (AuNPs) have gained increasing attention as diagnostic and therapeutic tools in ophthalmology due to their strong absorption and scattering of incident light through surface plasmon resonance.[1–3] In ophthalmic imaging, AuNPs are used as contrast agents for optical coherence tomography and photoacoustic imaging.[1] In ophthalmic therapy, AuNPs are employed in drug delivery, gene therapy, anti-angiogenesis, and photothermal treatment.[2] Recent data suggest that AuNPs can potentially restore vision following the loss of photoreceptors, known to occur in retinitis pigmentosa and age-related macular degeneration.[3] Upon shining near-infrared light onto AuNPs attached to retinal ganglion cells (RGCs), the RGCs were activated, and visual perception was restored, as confirmed by monitoring neural responses in the mice visual cortex in vivo.[3]

An estimated 98% of pharmaceutic agents, including AuNPs, cannot cross the blood–retinal barrier (BRB), thus increasing the difficulty of treating retinal disorders.[4] Currently, delivering therapeutic agents to the eye involves invasive methods, such as intravitreal and subretinal injections, which pose risks such as inflammation, endophthalmitis, hemorrhage, retinal pigment epithelium (RPE) tears, and retinal detachment.[5,6] Delivering therapeutics, such as AuNPs, to the RGC layer using a non-invasive, safe, and efficient method remains an unmet need in the ophthalmic field.

Recently, focused ultrasound (FUS) combined with intravenously (IV) administered microbubbles has gained attention for its potential to induce blood–brain barrier (BBB) modulation.[7–9] The interaction of FUS with microbubbles temporarily modifies tight junctions of the BBB to facilitate the passage of therapeutics administered in the blood to the brain.[10,11] FUS–BBB modulation is gaining momentum as a non-invasive, safe, controlled, and reversible technique to facilitate the delivery of IV-injected therapeutics to targeted brain areas, from animal models to clinical trials in patients with cancer, Parkinson disease, and Alzheimer disease.[7,12–16] Therapeutics that can benefit from FUS–BBB modulation delivery include drugs, biologics, recombinant adeno-associated viruses (AAVs), and nanoparticles.[17–19]

Considering that FUS–BBB modulation has been successful in delivering therapeutics from the blood to the brain at the preclinical and clinical stages, efforts have been made to similarly use FUS to modulate the BRB.[20] Park et al.[21] first showed that the BRB can be transiently permeabilized using FUS. Touahri et al.[22] subsequently demonstrated that FUS can be used in rodents to deliver intravenously administered AAV8 across the BRB, resulting in Müller glia gene transduction. To date, only AAVs and magnetic resonance imaging (MRI) contrast agents have been shown to cross the BRB using FUS, and FUS-assisted delivery of metallic nanoparticles into the retina has not yet been reported.

In the current study, we optimized FUS parameters for the delivery of IV-injected AuNPs across the BRB and into the RGC layer. As the geometry of AuNPs is the crucial factor that determines their therapeutic and diagnostic effects, we evaluated the ability of FUS to deliver AuNPs of different sizes and shapes. Label-free imaging of AuNPs embedded in the retina was thoroughly investigated to quantitatively evaluate FUS-mediated AuNP delivery. We performed further evaluations of the degree and location of injection, including histological analyses, to ensure the safety of the method.

Methods

Animal Preparation

All animal experimental procedures were approved by the Institutional Animal Care and Use Committee (2021-0171) of Yonsei University (Seoul, Republic of Korea). A total of 27 C57BL/6 male mice (9 weeks old, 20–25 g) were housed in groups of five in each cage under a 12-hour light/dark cycle in a room with controlled temperature (22°C ± 2°C) and humidity (55% ± 5%), and they were provided ad libitum access to food and water. The number of animals per group used in each study was as follows: MRI ($n = 6$), dextran ($n = 6$), 10-nm AuNP ($n = 5$), 55-nm AuNP ($n = 5$), and 40 × 80-nm gold nanorods (AuNRs; $n = 5$).

Characterization of Dextran and AuNPs

The zeta potential and hydrodynamic sizes of dextran (D1818; Thermo Fisher Scientific, Waltham, MA) and AuNPs (Ntracker; Nanopartz, Loveland, CO) were analyzed using a particle size analyzer (Zetasizer Nano ZS; Malvern Panalytical, Malvern, Worcestershire, UK). In-depth data regarding the size of AuNPs (gold nanospheres [AuNSs] and AuNRs) were obtained using a transmission electron microscope (TEM; JEM-3011 HR; JEOL, Tokyo, Japan). The absorption spectra (400–1100 nm) of all AuNPs were measured using an ultraviolet (UV)-visible spectrophotometer (MEGA-800; SCINCO, Seoul, Republic of Korea).

Downloaded from tvst.arvojournals.org on 11/11/2024

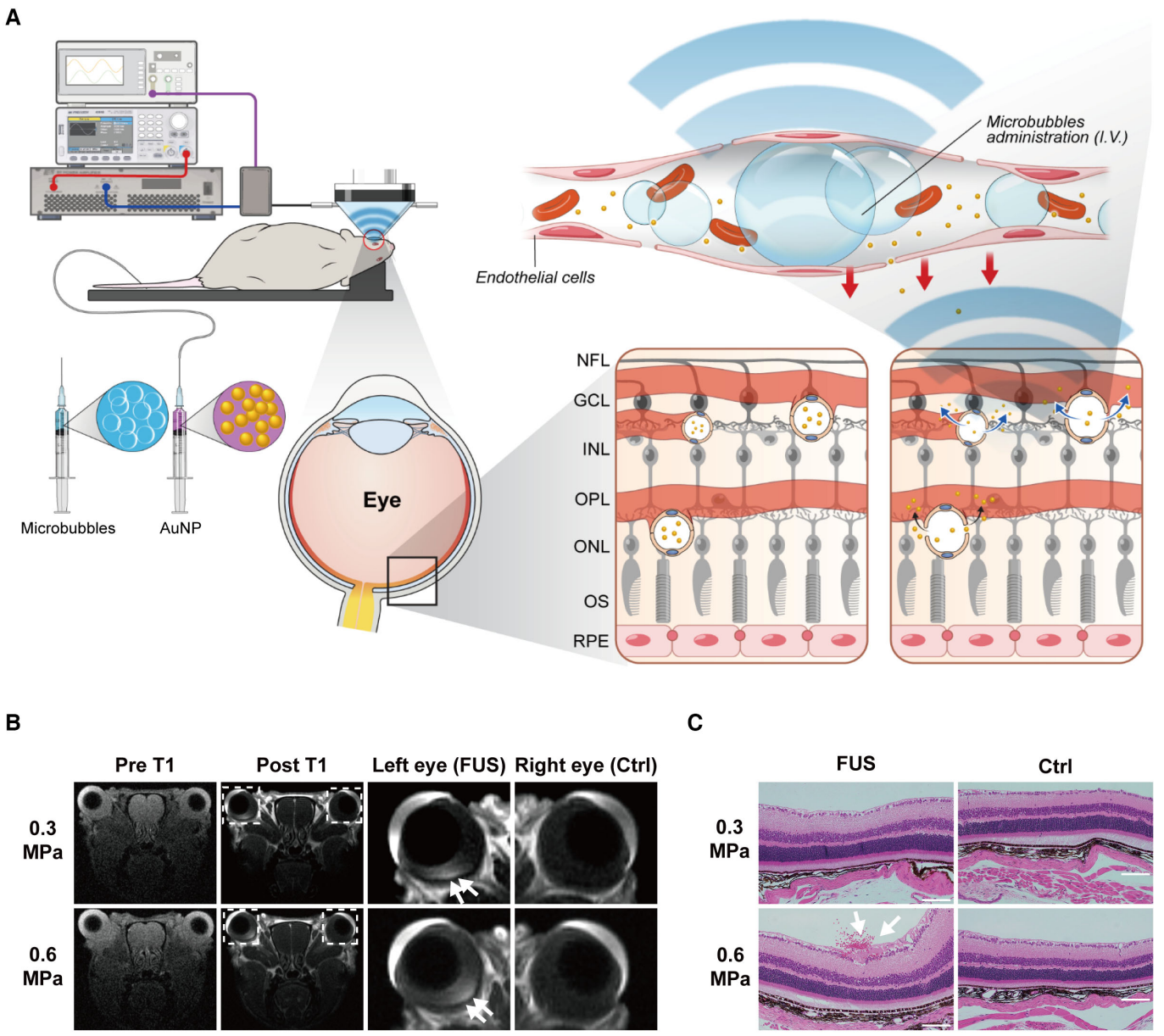


Figure 1. FUS and verification of safe modulation of the BRB via FUS. (**A**) Experimental setup of FUS-mediated retinal delivery of gold nanoparticles. Microbubbles and particles were intravenously injected, and the left eye was targeted with FUS. (**B**) Representative T1-weighted MRI of the mouse eye after sonication at 0.3 MPa and 0.6 MPa. No signal variation was observed between the left and right retina for pre-T1 images for both 0.3 and 0.6 MPa. For the post-T1 images, BRB-modulation—gadolinium enhancement in the left eye (zoomed image of left eye [FUS], *arrows*)—is observed compared to the right eye (zoomed image of right eye [Ctrl]). Zoomed image of left eye (FUS) images indicate the bright peak near the fundus (*white arrow*), suggesting that gadolinium bypassed the BRB where FUS was targeted for both levels of FUS energy applied. (**C**) Representative H&E images of the mouse eye at 0.3 MPa and 0.6 MPa. The *white arrow* indicates the occurrence of hemorrhage using 0.6 MPa energy. *Scale bar*: 50 µm.

Focused Ultrasound With Microbubbles

A waveform generator (33220A; Agilent, Palo Alto, CA) was connected to a 50-dB radiofrequency (RF) power amplifier (240 L; ENI Technology, Rochester, NY) to drive the FUS transducer (Fig. 1A). A 515-kHz, single-element, spherically focused transducer (H-107MR; Sonic Concept, Bothell, WA) with a diameter of 51.7 mm and radius of curvature of 63.2 mm was used to generate pulsed ultrasound. A coupler (C30-102-481/2N; Pulsar Microwave, Clifton, NJ) was used to connect the power amplifier and transducer. The consistency of the RF signal fed into the transducer was continuously monitored using

translational vision science & technology

Downloaded from tvst.arvojournals.org on 11/11/2024

an oscilloscope (DSOX2002A; Keysight Technologies, Santa Rosa, CA). The transducer was mounted on a cone filled with degassed water, and the end of the tip was wrapped in a polyurethane membrane. The acoustic beam profile was measured in a tank filled with degassed water by using a needle-type hydrophone (HNA-0400; Onda Corporation, Sunnyvale, CA). The fundamental frequency used to drive the transducer was 515 kHz, and the output pressure in response to the input voltage was measured (Supplementary Table S1). The full width at half maximum and the focal depth of the acoustic beam were 4 mm and 51.74 mm, respectively.

Before sonication, the animals were anesthetized with a mixture of ketamine (75 mg/kg), xylazine (Rompun, 4 mg/kg; Dechra Veterinary Products, Northwich, UK), and acepromazine (0.75 mg/kg) and were placed on a custom bed, lying on their left side to target the eye (Fig. 1A). Ultrasound gel (ProGel; Dayo Medical Co., Seoul, Republic of Korea) was used to fill the gap between the animal's eye and cone tip to maximize the transmission efficiency of the ultrasound. All nanomaterials were diluted with 0.9% normal saline to obtain a final concentration of 1 mg/mL for dextran and 20 μg/μL for AuNPs. The nanomaterials were IV administered via a tail vein catheter. Immediately after nanomaterial injection, saline-diluted microbubbles (DEFINITY; mean diameter range, 1.1–3.3 μm; Lantheus Medical Imaging, North Billerica, MA) were IV administered using the same catheter. After 10 seconds of microbubble injection, bursts of sonication were applied to the left eyes of animals. The right eyes of animals that were not sonicated were used as controls. Sonication parameters were set as follows: burst duration, 10 ms; pulse repetition frequency, 1 Hz; total duration, 120 seconds; and two different average peak-negative pressures, 0.3 and 0.6 MPa.

Magnetic Resonance Imaging

While performing MRI, the animals were anesthetized using isoflurane (2%–2.5%) inhalation. MRI was performed 1 hour after sonication by using a Bruker 9.4 T MRI system (Biospec 94/20 USR; Bruker, Ettlingen, Germany) and a mouse brain surface coil. Gadobutrol (Gadovist; Bayer, Leverkusen, Germany), a gadolinium-based MRI contrast agent, was IV administered at a concentration of 0.2 mL/kg. Contrast-enhanced T1-weighted images (echo time, 8.06 ms; repetition time, 500 ms; echo train length, 2 ms; slice thickness, 0.3 mm) were captured with and without contrast medium injection.

Tissue Preparation

All animals used in this study were perfused 4 hours after sonication with 0.9% normal saline, followed by 4% paraformaldehyde in 1× phosphate-buffered saline (PBS). Subsequently, we performed ocular enucleation, following which we prepared two types of tissue samples—namely, paraffin sections and whole-mount samples, which were used to obtain cross-sectional and whole-mount images, respectively. Paraffin sections were prepared for histology using hematoxylin and eosin (H&E) counterstains and for immunohistochemical staining. Eyeballs were fixed in 4% paraformaldehyde for 1 day and then sectioned to a thickness of 5 μm (parallel to the sonicated area) in a paraffin block. Deparaffinization and heat-mediated antigen retrieval were performed using 1× citrate buffer (boiling for 15 minutes at 85°C, followed by cooling down for 30 minutes). Before each step, the sample was washed in 1× PBS. In addition, to analyze the dextran and AuNP distribution across the RGC layer, retinal whole-mount samples were prepared. The eyes were fixed with 4% paraformaldehyde for an additional 1 hour and then collected in a dish filled with 1× PBS. A binocular microscope was then used for retinal dissection as follows: Spring scissors were used to remove the optic nerves behind the eyes and the short debris of the sclera around them, the limbus of the eye was cut with the scissors, and subsequently the anterior segments of the eye (cornea and ciliary body) were separated. Forceps were used to extract the lens from the posterior segment, and the sclera, along with the underlying choroid, was excised to detach it from the retina. The rest of the eyecup contained the retina, which appeared smooth and opaque. To release the retina, two pairs of micro-forceps were used to remove the remaining choroid and excess tissue and lightly pressed to separate the retina. Four incisions were made to flatten the retina with micro-scissors, excess PBS was removed using a wide-diameter plastic Pasteur pipette, and the eyecup was spread like a flower.[23]

Immunohistochemical and Histological Analyses

The retinal samples were blocked for 2 hours at room temperature (20°C) in a blocking solution containing PBS, 0.2% normal goat serum, and 0.2% Triton X-100. Subsequently, the retinas were incubated overnight at 4°C in a blocking solution containing rabbit polyclonal anti–RNA-binding protein with multiple splicing (RBPMS) antibody (1:500, ab152101; Abcam, Cambridge, UK), which is selectively expressed in RGCs.[24,25] After the primary

Downloaded from tvst.arvojournals.org on 11/11/2024

immunoreaction, the samples were briefly washed with 1× PBS and incubated for 2 hours at room temperature with goat anti-rabbit secondary antibodies (1:1000; A-21071; Thermo Fisher Scientific) conjugated with Alexa Fluor 633. The nuclei were stained with 4′,6-diamidino-2-phenylindole (DAPI; 1:1000, D1306; Thermo Fisher Scientific) during conjugation with secondary antibodies.

Hematoxylin (VectorLabs, Newark, CA) and eosin (Sigma-Aldrich, St. Louis, MO) staining was performed on paraffin sections, and brightfield images of the sectioned samples were acquired using an optical microscope (BX51; Olympus, Tokyo, Japan). Histological analysis was performed to examine retinal tissue damage, especially near the blood vessels, and to monitor for any indications of red blood cell extravasation.

Confocal Microscopy

The distribution of dextran injected in the retina was visualized using a confocal laser scanning microscope (LSM980; Carl Zeiss Microscopy, Wetzlar, Germany) within the spectrum of visible light. Laser wavelengths of 345, 633, and 555 nm were used to excite the fluorescence of DAPI, Alexa Fluor 633, and dextran, respectively (Table 1). Emissions at each excitation wavelength were recorded in the multitracking mode, using a combination of three separate detection channels within the fixed spectral band. To obtain the full image of dextran distribution across the RGC layer, tile scans were performed using a 2.5× objective lens. Cross-sectional retinal images were captured using a 20× objective.

Two-Photon Microscopy

AuNPs were visualized by imaging the two-photon luminescence (TPL) of AuNPs with two-photon microscopy (2PM; LSM 780 NLO; Carl Zeiss Microscopy, Korea Basic Science Institute in Seoul center) within the spectrum of near-infrared light.[26,27] Before AuNPs injected into the retina were imaged, optimum parameters, such as the excitation wavelength and power/gain for TPL visualization, were investigated. The optimum excitation wavelength was determined at the point where the TPL of AuNPs was maximized. In the current study, three different types of AuNPs were employed: spherical AuNPs, with diameters of 10 nm (0.33 mg/mL) and 55 nm (0.35 mg/mL), and rod-shaped AuNPs (0.38 mg/mL), with height and width of 80 nm and 40 nm, respectively. Diluted AuNPs (10 µL) were sandwiched between a slide glass and coverslip and imaged while scanning

Table 1. Microscopy Parameters

Nanomaterial	Microscope	Objective Lens (NA)	Field of View	Excitation Wavelength	Detection	Laser Power	Detection Mode	Detection Gain	Detection Offset
Dextran, 70 kDa	Confocal microscope	2.5 × (0.085)	6.4 × 6.4 mm	561 nm (dextran, 555 nm)	Fluorescence	2%	Channel (543–614 nm)	850	−50
AuNS, 10 nm	Two-photon microscope	40 × (1.2)	212.55 × 212.55 µm	720 nm	Two-photon luminescence	6%	Channel (498–612 nm) Lambda (415–686 nm; interval, 9 nm)	950	N/A
AuNS, 55 nm	Two-photon microscope	40 × (1.2)	212.55 × 212.55 µm	720 nm	Two-photon luminescence	6%	Channel (498–612 nm) Lambda (415–686 nm, interval: 9 nm)	950	N/A
AuNR, 40 × 80 nm	Two-photon microscope	40 × (1.2)	212.55 × 212.55 µm	750 nm	Two-photon luminescence	6%	Channel (498–612 nm) Lambda (415–686 nm; interval, 9 nm)	950	N/A

N/A, not applicable.

Downloaded from tvst.arvojournals.org on 11/11/2024

the excitation wavelengths from 690 to 790 nm, with an interval of 10 nm. One of the main challenges faced during imaging AuNPs injected into retinal tissue was that the TPL signal from AuNPs might be buried in the autofluorescence signal of the retinal tissue. Hence, we investigated the allowable range of power and gain for AuNP detection while avoiding TPL signals from the bare retinal tissue. The minimum threshold 2PM laser source power and gain for obtaining TPL signals were determined for both nanoparticles and retinal tissue. The selected power and gain were greater than the threshold for AuNP detection but were maintained at lower levels than those for the retinal tissue to rule out possible autofluorescence acquisition from the retinal tissue. Optimum 2PM excitation wavelength and power/gain were exploited for AuNP visualization.

When the AuNP-containing retinal samples were imaged, the following factors were taken into account to prevent autofluorescence capture in the images: First, TPL autofluorescence of the retinal tissue begins to appear at the RGC layer and increases toward the photoreceptor layer,[28] so the imaging plane was maintained near the upper part of the RGC layer to prevent strong TPL autofluorescence. Second, the TPL spectrum was compared with those of retinal tissue and AuNPs because their TPL emission spectra have their own distinct shapes.[29] We obtained images by using optimum 2PM parameters, followed by post-image processing (Table 1). Subsequently, the images for which the TPL spectra resembled those of RGCs were discarded.

Data Analysis

All statistical analyses were performed using MATLAB R2020b (MathWorks, Natick, MA). The signal intensity of dextran was summed for statistical analysis. Student's *t*-test was used to determine the statistical significance of dextran delivery into the retina by FUS compared to that obtained without FUS application. In the TPL images of the AuNPs, noise and possible autofluorescence from the retinal tissue were first removed and the signal intensity was summed in the same manner as for dextran. To exclude noise and autofluorescence from the retinal tissue, the background noise level was determined by obtaining the average intensity from the region that did not have any AuNPs, which could be confirmed by the TPL emission spectrum. We then set the threshold as n (multiplicative factor) times the background noise level, and the TPL signals below the threshold value were removed. Because the background noise level varied between samples (Supplementary Fig. S1), we slightly changed the multiplicative factor ($n \sim 2$) for the samples after confirming the removal of the noise signal. The TPL data were analyzed using one-way analysis of variance (ANOVA) followed by Tukey's post hoc test, which was used to determine differences between experimental groups. $P < 0.05$ was considered statistically significant for both dextran and AuNPs.

Results

Evaluation of FUS Parameters and BRB Modulation

To confirm whether FUS can permeabilize the BRB, MRI was conducted before and after the administration of gadolinium contrast agent (~650 Da) (Fig. 1A). At 1 hour after FUS application to the left eye, a T1 contrast-enhanced image was obtained without injecting the contrast agent (Fig. 1B, pre-T1 image). Nearly uniform brightness across the retinal layer was observed, with no difference between the right and left eyes. We obtained another T1 contrast-enhanced image after injecting gadolinium (i.e., post-T1 image). For FUS at both 0.3 and 0.6 MPa, we found bright spots only on the left eyes (i.e., Fig. 1B, zoomed image of left eye [FUS] with white arrow) but no bright peaks on the right eyes. These results indicate that the BRB inside the retinal layer was permeabilized due to FUS, thus allowing gadolinium to leak out into the vitreous humor.

After identifying that a FUS exposure of 0.3 MPa was sufficient for BRB permeabilization, we determined the FUS pressure that could be used without causing retinal damage. The H&E findings showed that tissue damage did not occur with a FUS exposure of 0.3 MPa, which is consistent with the results in the control group where sonication was not used (Fig. 1C). In contrast, a FUS exposure of 0.6 MPa led to the detection of hemorrhage, suggesting the rupture of the vasculature, near the RGC layer (i.e., FUS with 0.6-MPa image with white arrow) compared to the right eye. In conclusion, FUS exposures of 0.3 and 0.6 MPa resulted in FUS-induced BRB permeability; however, based on H&E analyses, it is recommended that a 0.3-MPa FUS exposure should be used to avoid damage and ensure a safe sonication procedure.

Dextran Efficiently Reached the RGC and Inner Nuclear Layers

After determining the FUS parameters capable of achieving BRB permeabilization without retinal tissue damage, we set out to establish whether nanomaterials in the size range of 16 to 80 nm with different materials

Downloaded from tvst.arvojournals.org on 11/11/2024

Table 2. Zeta Potential, Hydrodynamic Radius, and Polydispersity Index

		AuNSs		
	Dextran, 70 kDa	10 nm	55 nm	AuNR, 40 × 80 nm
Zeta potential	−1.15 mV	−16.4 mV	−21.5 mV	−7.9 mV
Hydrodynamic radius	16 nm	59.02 nm	83.3 nm	27.8 nm
Polydispersity index	0.301	0.381	0.193	0.399

(organic compound and metal) and shapes (spherical and rod) can cross the BRB. We first evaluated whether nanomaterials smaller than 20 nm in diameter and 70 kDa in weight can be delivered to the retinal tissue via FUS and determined their distribution across the retinal layers. We employed dextran because it is available in a wide range of defined sizes and can be easily visualized using confocal microscopy.[25,30] The electrical and physical properties of dextran were characterized before injection for FUS delivery. The zeta potential of 70-kDa dextran was found to be −1.15 mV; dynamic light scattering (DLS) measurement revealed a hydrodynamic diameter of 16 nm, with a polydispersity index of 0.301 (Table 2).

Confocal microscopy was performed on harvested retinas to investigate the ability of FUS to facilitate the passage of particles across the BRB using 70-kDa dextran. Dextran distribution across the RGC layer was visualized in whole-mount retinas (Fig. 2A). A robust tetramethylrhodamine signal (excitation and emission of 555 nm and 580 nm, respectively; fluorescent dye conjugated to 70-kDa dextran) was noted in the fundus of the retina. The dextran signal was colocalized with immunolabeled RBPMS, an RGC-specific marker, thus confirming dextran delivery to the RGC layer. Furthermore, cross-sectional images revealed the delivery of dextran to the RGC layer (Fig. 2B, FUS sample 1, white arrow) and the inner nuclear layer of the retina (Fig. 2B, FUS sample 2, white arrow). We speculate that the variation in the dextran distribution along the retinal layer stems from differences in the blood vessel distribution within the limited imaging area (227 µm × 265 µm). Notably, the dextran signal was not detected across the retinal layers in samples not subjected to FUS treatment. The cross-sectional and whole-mount images confirm the local distribution of dextrans in the RGC layer. Additionally, morphological analyses showed that the FUS treatment and dextran injection did not lead to tissue damage; no hemorrhages were detected. Statistical analyses of whole-mount samples confirmed that the amount of 70-kDa dextran (size, 16 nm; experimental group (EXP): 6.98 a.u. ± 1.33 a.u.) that crossed the BRB following FUS application was seven times greater than that achieved without FUS (control, 1.00 a.u. ± 0.31 a.u.; $P < 0.05$ compared to the control; $n = 3$ for each group) (Fig. 2C).

To further confirm whether the dextran signal detected originated from the dextran that had passed the BRB and not from the dextran inside blood vessels, we investigated whether blood perfusion had completely washed out the dextran remaining in the blood vessels. We did not detect any dextran signal for the samples that had been subjected to blood perfusion (Fig. 2D, left). However, a vascular-shaped dextran signal was noted for the samples for which blood perfusion had not been performed, indicating that dextran was stuck inside the blood vessels with no blood perfusion (Fig. 2D, right, white arrow). The samples shown in Figure 2D provide examples of retinas that were not sonicated using FUS. Collectively, these results showed that 70-kDa dextran could selectively cross the BRB at the RGC and inner nuclear layer via FUS treatment without damaging the retina.

Two-Photon Luminescence of AuNPs

The results of the intravenous injection of dextran indicated the potential use of FUS for delivering tens of nanometer-sized nanomaterials. To our knowledge, the delivery of metallic nanomaterials of various sizes and shapes has not yet been studied using FUS delivery. Hence, we first sought to identify the optimum imaging methodology for AuNPs in retinal samples. Before the FUS experiment, we characterized the electrical and physical properties of AuNPs. In this study, we used both AuNSs and AuNRs. Representative TEM images of three types of AuNPs are shown in Figure 3A. The average diameters of small (10 nm) and large (55 nm) AuNSs were 10.8 nm and 56.7 nm, respectively. The height and length of AuNRs (40 × 80 nm) that had approximately the same volume as the large AuNSs were 39.7 nm and 80.7 nm, respectively. Hydrodynamic size distributions, as measured by DLS, are also shown in Table 2. The zeta potentials for 10-nm AuNSs, 55-nm AuNSs, and 40 × 80-nm AuNRs were −16.4, –21.5, and –7.9 mV, respectively (Table 2). A UV-visible (Vis) spectrophotometer was also used to

Downloaded from tvst.arvojournals.org on 11/11/2024

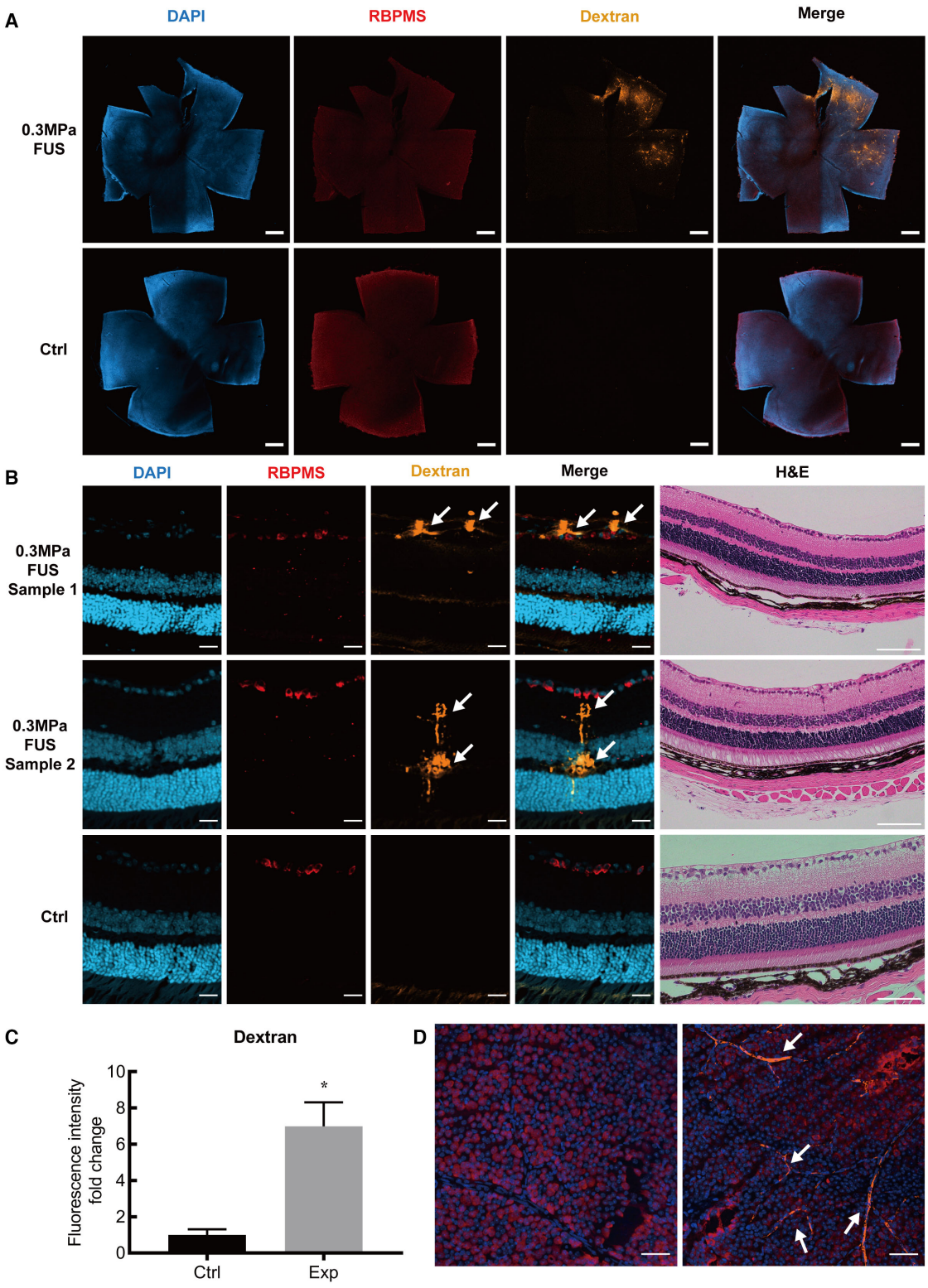


Figure 2. Detection of dextran signal in the retinal ganglion cell layer and inner nuclear layers after FUS. (**A**) Representative flatmount immunofluorescence image of DAPI (*blue*), RBPMS *red*), and 70-kDa dextran (*orange*). *Scale bar*: 500 µm. (**B**) Representative cross-sectional fluorescence images of DAPI (*blue*), RBPMS (*red*), 70-kDa dextran (*orange*), and H&E staining. *Scale bar*: 50 µm. (**C**) Bar graphs showing fold changes in the intensity of 70-kDa dextran in the ganglion cell layer of the experimental group relative to those in the control. Data represent mean ± SEM values. Statistical analyses were performed using the unpaired *t*-test (*$P < 0.05$ compared with control). (**D**) Representative immunofluorescence images of dextran in the mouse eye. The dextran in the blood vessel (*white arrow*) can be seen depending on whether perfusion was performed (*left*) or was not performed (*right*). *Scale bar*: 50 µm.

Downloaded from tvst.arvojournals.org on 11/11/2024

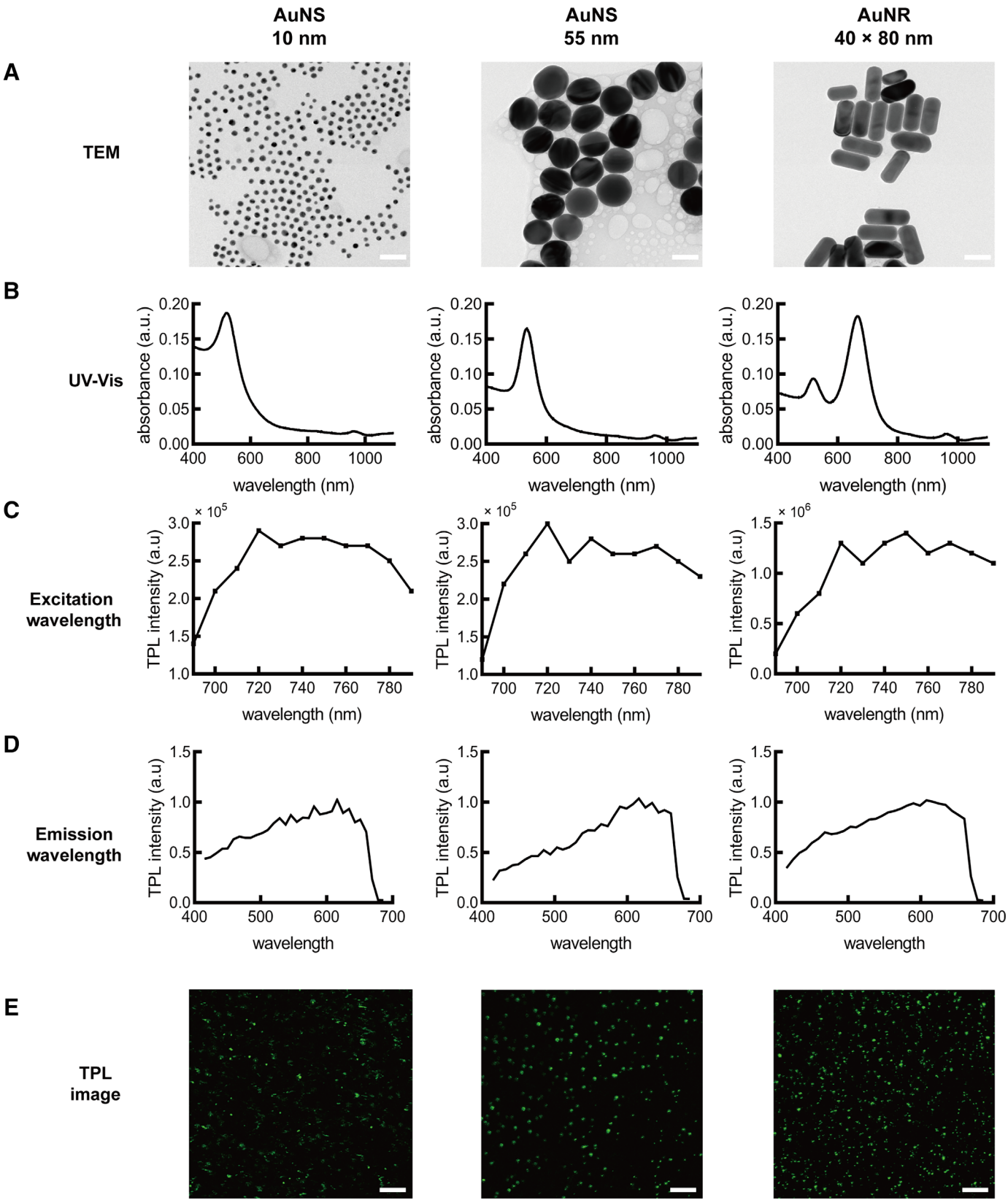


Figure 3. Characterization of AuNPs. (**A**) Representative TEM images of 10-nm AuNSs (*left*), 55-nm AuNSs (*middle*), and 40 × 80-nm AuNRs (*right*). *Scale bar*: 50 µm. (**B**) UV-Vis graph of 10-nm AuNSs (*left*), 55-nm AuNSs (*middle*), and 40 × 80-nm AuNRs (*right*). (**C**) Excitation wavelength graph of 10-nm AuNSs (*left*), 55-nm AuNSs (*middle*), and 40 × 80-nm AuNRs. (**D**) Emission wavelength graph of 10-nm AuNSs (*left*), 55-nm AuNSs (*middle*), and 40 × 80-nm AuNRs (right). (**E**) Representative TPL image of 10-nm AuNSs (*left*), 55-nm AuNSs (*middle*), and 40 × 80-nm AuNRs (*right*). *Scale bar*: 10 µm.

Downloaded from tvst.arvojournals.org on 11/11/2024

characterize the absorption spectrum of these particles. We found that the 10-nm and 55-nm AuNSs showed localized surface plasmon resonance (LSPR) peaks at 516 nm and 534 nm, respectively, and the 40 × 80-nm AuNRs showed transverse and longitudinal LSPR peaks at 518 nm and 666 nm, respectively (Fig. 3B).

We employed a 2PM for imaging AuNPs. Initially, optimum values for parameters such as excitation wavelength, emission wavelength, and power/gain of 2PM were investigated. When determining the optimum excitation wavelength, the total TPL intensity of the AuNPs was measured over various excitation wavelengths ranging from 690 to 790 nm. The wavelength where the maximum TPL intensity was obtained was selected as the optimum excitation wavelength. The optimum excitation wavelengths for AuNSs of 10 and 55 nm and AuNRs of 40 × 80 nm were 720 nm, 720 nm, and 750 nm, respectively (Fig. 3C). Next, the optimum emission wavelength for image acquisition was determined. The emission spectra were acquired after illuminating AuNPs at the optimum excitation wavelength determined above (Fig. 3D). The emission spectra of all the AuNPs had similar shapes in that their emission spectra near-linearly increased as wavelength increased and maximized around 612 nm. After reaching their maximum point, the spectra rapidly decayed and diminished before reaching 686 nm. Hence, the emission channels for imaging TPL signals were set from 498 to 612 nm. Next, appropriate laser settings such as the gain and percentage of output laser power were determined in a way to acquire a high signal-to-noise ratio. We set the laser output percentage at 6% (maximum power: 2083.1 mW and 2715.6 mW for 720 nm and 750 nm, respectively) and gain at 950 for all nanoparticles.

Monodispersed grainy TPL patterns were monitored (Fig. 3E). However, the pattern size showed some variation, indicating that some particles aggregated in varying numbers (Supplementary Fig. S3). Moreover, upon a constant weight concentration, the summed TPL intensity for the 10-nm and 55-nm AuNSs was almost the same, but that of the 40 × 80-nm AuNRs was ~1.8 times greater than that of the other particles (Supplementary Fig. S4). Meanwhile, the absolute number of particles per unit volume for the 10-nm AuNPs was 157 times greater than that of the 55-nm particles and 142 times greater than that of the 40 × 80-nm particles. We speculated that the discrepancy in the measured TPL intensity versus the number of particles upon a constant weight concentration originated from the difference in the 2PM imaging capability for particles of different sizes and shapes.

FUS Delivered AuNPs to the RGC

After optimizing the parameters for AuNPs in 2PM, we administered AuNPs of various sizes and shapes into the retina using FUS and visualized their distribution in the RGC layer using 2PM. Brightfield images were superimposed on TPL images to examine the distribution of AuNPs in the RGC layer. We swept across the RGC layer to acquire images where the AuNPs were located. We found that AuNPs were observed in the RGC layer after FUS for all AuNPs (Fig. 4A, exemplar signals indicated by arrows). For the 10-nm AuNSs, agglomerated strong TPL signals were observed, which indicated that some AuNSs were aggregated (Fig. 4A, inside broken line box 1). Nonaggregated 10-nm AuNSs were also visible but had low intensity (Fig. 4A, inside broken line box 2). Importantly, we confirmed that the TPL signal originated from the AuNPs and not from the retina, as the TPL spectra (Fig. 4B) resembled those obtained for bare AuNPs (Fig. 3C).

Figure 4C shows the histogram for TPL intensity of the AuNPs with and without FUS. All FUS-treated experimental groups (10-nm AuNS, $3.93 \times 10^4 \pm 1.35 \times 10^4$; 55-nm AuNS, $5.4 \times 10^3 \pm 1.75 \times 10^3$; 40 × 80-nm AuNR, $0.72 \times 10^5 \pm 0.25 \times 10^5$) showed significantly higher intensity than the control groups that had not been subjected to FUS (control for 10-nm AuNS, $0.07 \times 10^4 \pm 0.01 \times 10^4$; control for 55-nm AuNS, $0.07 \times 10^3 \pm 0.01 \times 10^3$; control for 40 × 80-nm AuNR, $0.01 \times 10^5 \pm 0.005 \times 10^5$; $P < 0.05$ compared with each control; $n = 3$ for each group). These results demonstrate that spherical and rod-shaped AuNPs with a maximum dimension of 80 nm could bypass the BRB when FUS was used, whereas BRB efficiently blocked AuNPs with a minimum dimension greater than 10 nm when FUS was not used. The degree of AuNP delivery to the RGC layer after FUS was also compared (Fig. 4D). Although AuNPs were IV injected at the same weight concentration (20 μg/μL), the TPL intensity of bare AuNPs for the same weight concentration was not constant (Supplementary Fig. S4); hence, for a fair comparison, the TPL intensity acquired from AuNPs with retinal samples was normalized to the TPL intensity of bare AuNPs obtained at the same weight concentration. The normalized TPL intensity of 10-nm AuNSs was 16.9 times greater than that of 55-nm AuNSs and 4.8 times greater than 40 × 80-nm AuNRs ($P < 0.05$ compared to the 55-nm AuNSs and 40 × 80-nm AuNRs). We speculated that the small nanoparticles have higher permeability to the BRB after FUS than big nanoparticles. Moreover, morphological damage, especially hemorrhage, was not observed in either the FUS-treated or untreated

Downloaded from tvst.arvojournals.org on 11/11/2024

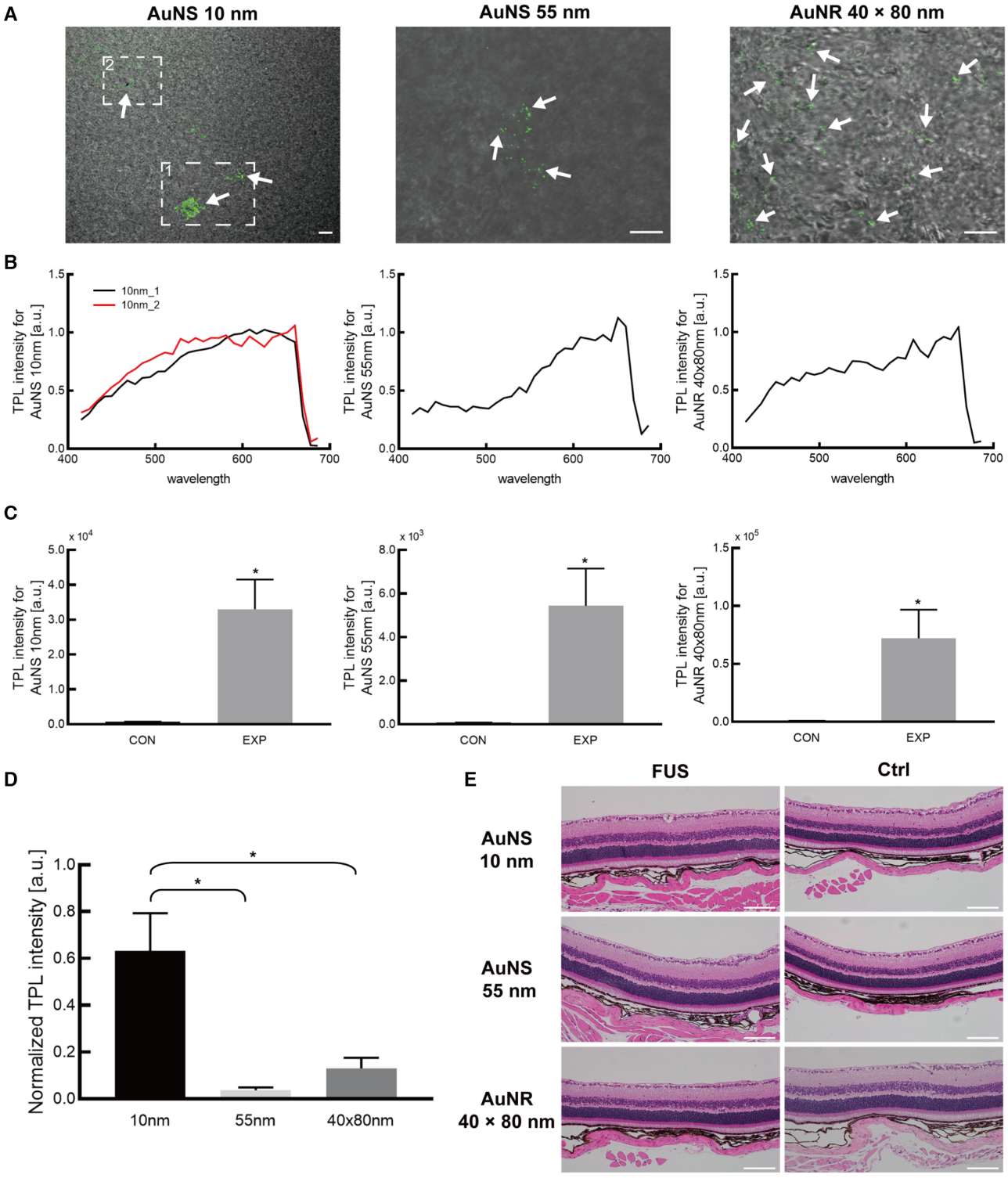


Figure 4. FUS-based delivery of AuNPs to the retinal ganglion layer. (**A**) Representative TPL images merged with brightfield images for 10-nm AuNSs (*left*), 55-nm AuNSs (*center*), and 40 × 80-nm AuNRs (*right*) in the experimental group. *Scale bar*: 10 µm. (**B**) TPL emission wavelength spectrum for 10-nm AuNSs (*left*), 55-nm AuNSs (*center*), and 40 × 80-nm AuNRs (*right*) in the brightfield image. (**C**) Bar graphs showing particle intensity in the experimental group relative to that in the control. Data are shown for 10-nm AuNSs (*left*), 55-nm AuNSs (*center*), and 40 × 80-nm AuNRs (*right*) and are presented as mean ± SEM values. Statistical analyses were performed using the unpaired *t*-test (*$P < 0.05$ compared with control). (**D**) Bar graphs showing particle intensity in the experimental group. Data represent mean ± SEM values. Statistical analyses were performed using a one-way ANOVA with Tukey's multiple comparison test (*$P < 0.05$; $n = 3$ for each group). (**E**) Representative H&E images of the mouse eye. *Scale bar*: 50 µm.

Downloaded from tvst.arvojournals.org on 11/11/2024

samples (Fig. 4E). Taken together, these results demonstrate that both AuNSs and AuNRs significantly cross the BRB 4 hours after FUS in mice compared to those without FUS.

Discussion

In this study, we investigated FUS-assisted delivery of AuNPs of varying sizes and shapes to retinal tissue for the first time, to our knowledge. As AuNPs provide both therapeutic and diagnostic benefits related to retinal diseases, the delivery of AuNPs non-invasively has clinical significance. We investigated not only the clinical benefits in the field of ophthalmology but also the scientific implications, especially label-free imaging of various AuNPs that are embedded in the retinal tissue.

We demonstrated that FUS effectively modulates the BRB, primarily through microbubble cavitation within the blood vessels. This process, facilitated by the interaction of FUS with ultrasound waves, plays a crucial role in altering the properties of the BRB. Prior to FUS application, it is essential to first align the transducer with the eye to ensure that the ultrasound beam is focused on the target retina tissue. Although our transducer is designed for easy three-dimensional focusing, an additional monitoring system that enables precise monitoring of depth of focus when FUS is directed toward retinal tissue must be developed. In addition, a new stereotactic tool for FUS treatment of the mice eye should be developed. Such developments could prevent issues such as images being out of focus and BRB impermeability.

The transient permeabilization of the BRB using FUS has been demonstrated in rodents. However, a comprehensive quantitative analysis of sonication parameters, which enables effective modulation without causing tissue damage, requires further investigation, especially in mice.[21,22] Among the various adjustable FUS parameters, such as pulse repetition rate, pulse repetition frequency, and pressure, the acoustic pressure amplitude applied to the tissue is one of the critical determinants of both tissue damage and permeability.[11,31–33] The careful manipulation of this parameter is thus crucial in ensuring the safety and efficacy of FUS-based therapeutic strategies.

In this study, we first optimized the allowable FUS pressure that would permeabilize the BRB without damaging the retina tissue in the rodent model of mice. We found that FUS pressure of 0.6 MPa induces not only BRB permeability but also retinal tissue damage. The impact of FUS on tissue damage is not solely determined by the pressure exerted by FUS but can also be affected by multiple factors such as microbubble characteristics, the physical structure and dimension of the eye, and the microvasculature structure.[11,34,35] As a result, adjusting these variables can alter the level at which retinal damage occurs. Although we demonstrated the potential of FUS as a method for modulating the BRB, the safety analysis was not performed simultaneously during sonication. As FUS intensity applied to the retina varies due to the variation in focusing, the exact point when the microbubble sufficiently cavitates without retina tissue damage may vary. Therefore, the application of simultaneous control mechanisms, such as a passive cavitation detector, holds the potential to enable more precise and safer application of FUS to control BRB.

When imaging dextran in the retina sample, dextran signal was observed even without FUS. We speculate that the signal acquired in the control group (without FUS) may have originated from the background noise and/or autofluorescence of the retinal tissue itself and/or the actual fluorescence signal from the dextran. For quantitative analysis, confocal images were captured under identical image acquisition and processing settings (e.g., laser power, gain, and image processing settings) to achieve constant background noise and autofluorescence for all samples imaged.

We next investigated the appropriate imaging methodology to visualize AuNPs buried in the retinal tissue. First, we ruled out the fluorescent imaging of AuNPs conjugated with fluorescent dye, as the emission from the fluorescent dye may suffer from a quenching.[24] As bare AuNPs can be imaged using confocal microscopy and the 2PM method,[27,29,32,33] we compared the imaging capabilities of both methods. At first, a confocal microscope was employed, and its excitation and emission spectra were set to cover the LSPR peak of AuNPs. Unfortunately, the autofluorescence signal originating from the retinal tissue itself overwhelmed the scattered light signal from the AuNPs, indicating that the use of a confocal microscope was inappropriate for imaging AuNPs with retinal samples (Supplementary Fig. S2). The 2PM imaging, however, showed stronger TPL intensity for the AuNPs compared to the TPL intensity of bare retina, indicating that 2PM is an appropriate imaging method to visualize AuNPs embedded in the retina tissue.

As noted above, for 2PM imaging of AuNPs in the retina, it is important to consider the potential interference from autofluorescence signals produced by the retinal tissue itself. As shown in Supplementary Figure S5, strong TPL signal was observed when imaging the bare retina with a laser power and gain of 10.5% and

Downloaded from tvst.arvojournals.org on 11/11/2024

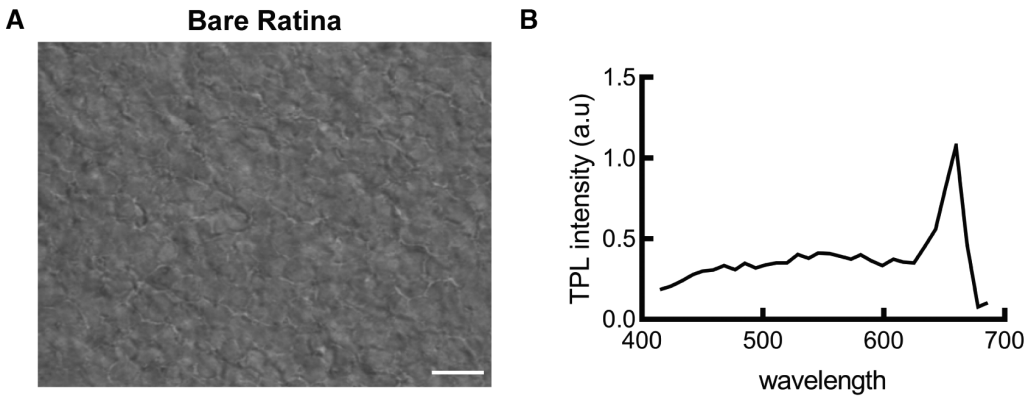


Figure 5. Characterization of bare retina. (**A**) Representative TPL image merged with brightfield image of the retina from the control group. *Scale bar*: 10 µm. (**B**) TPL emission wavelength spectrum for the bare retina in the brightfield image.

950, respectively. To selectively capture the TPL signal from the AuNPs while minimizing the retinal autofluorescence, the power and gain settings were adjusted. When imaging the bare retinal sample using identical laser settings (power and gain of 6% and 950, respectively) as those used to image the bare AuNPs, we found little retinal autofluorescence (Fig. 5). This result confirms that these laser settings are optimum to image AuNPs embedded in the retinal sample.

Our research primarily focused on the BRB and its direct response to FUS, so further research is needed to explore its effects on the outer blood–retinal barrier (oBRB), encompassing the RPE and choroid vasculature. Although our study did not experimentally confirm the effect of FUS on the oBRB, the possibility of its positive impact on this region is noteworthy. Future research should focus on validating these theoretical implications to fully understand the long-term effects of FUS-mediated BRB modulation. Longitudinal studies are essential to evaluate any sustained impacts on retinal functionality. Additionally, exploring the potential of integrating FUS-mediated nanoparticle delivery with other therapeutic approaches, such as gene therapy or pharmacological interventions, could lead to potential therapeutic strategies for retinal diseases.

Conclusions

The BRB is a critical physiological and anatomical barrier to retinal disease treatment. FUS-mediated BRB modulation is an emerging modality for the treatment of retinal diseases. As AuNPs are emerging as therapeutic and diagnostic agents in ophthalmology, methods must be developed to increase their accessibility to vulnerable retinal tissues. To the best of our knowledge, this study is the first to show that FUS can be used to deliver AuNPs of various sizes and shapes across the BRB without significant retinal damage. We identified optimized FUS parameters through histological analysis at different acoustic pressures. Further studies should be performed to develop this FUS technology to deliver multifunctional AuNPs for the treatment of retinal diseases. In summary, FUS-mediated delivery of AuNPs could represent a targeted and non-invasive approach for delivering therapeutic agents to the retina.

Acknowledgments

We thank Medical Illustration & Design, a part of the Medical Research Support Services of Yonsei University College of Medicine, for their excellent support with the medical illustrations.

Supported by grants from the National Research Foundation of Korea funded by the Korean Ministry of Science and ICT (2020R1C1C1010505, 2021R1A5A1032937, 2022R1C1C2006049); by the Korea Medical Device Development Fund (project no. RS-2020-KD000103); by a grant from the Korea Health Technology R&D Project via the Korea Health Industry Development Institute funded by the Ministry of Health and Welfare, Republic of Korea (HI19C1347); by BK 21PLUS Creative Human Resource Education and Research Programs for ICT Convergence in the 4th Industrial Revolution; and by 2022–2023 BK 21 FOUR Graduate School Innovation Support funded by the Pusan National University Global Fellowship program. This research was undertaken, in part, thanks to funding from the Canada

Downloaded from tvst.arvojournals.org on 11/11/2024

CIFAR AI Chairs Program, Tier 1 Canada Research Chair in Brain Repair and Regeneration, and a Dixon Family Chair in Ophthalmology Research to C.S.

Disclosure: **Y. Park**, None; **J. Shin**, None; **J. Park**, None; **S. Kim**, None; **J.H. Park**, None; **J. Kim**, None; **C.S. Kim**, None; **J.W. Chang**, None; **C. Schuurmans**, None; **I. Aubert**, None; **W.S. Chang**, None; **K. Eom**, None

References

1. Chen F, Si P, De La Zerda A, Jokerst JV, Myung D. Gold nanoparticles to enhance ophthalmic imaging. *Biomater Sci*. 2021;9:367–390.
2. Masse F, Ouellette M, Lamoureux G, Boisselier E. Gold nanoparticles in ophthalmology. *Med Res Rev*. 2019;39:302–327.
3. Nelidova D, Morikawa RK, Cowan CS, et al. Restoring light sensitivity using tunable near-infrared sensors. *Science*. 2020;368:1108–1113.
4. Yasukawa T, Ogura Y, Tabata Y, Kimura H, Wiedemann P, Honda Y. Drug delivery systems for vitreoretinal diseases. *Prog Retin Eye Res*. 2004;23:253–281.
5. Peyman GA, Lad EM, Moshfeghi DM. Intravitreal injection of therapeutic agents. *Retina*. 2009;29:875–912.
6. Falavarjani KG, Nguyen QD. Adverse events and complications associated with intravitreal injection of anti-VEGF agents: a review of literature. *Eye (Lond)*. 2013;27:787–794.
7. Lipsman N, Meng Y, Bethune AJ, et al. Blood–brain barrier opening in Alzheimer's disease using MR-guided focused ultrasound. *Nat Commun*. 2018;9:2336.
8. Abrahao A, Meng Y, Llinas M, et al. First-in-human trial of blood-brain barrier opening in amyotrophic lateral sclerosis using MR-guided focused ultrasound. *Nat Commun*. 2019;10:4373.
9. Gasca-Salas C, Fernández-Rodríguez B, Pineda-Pardo JA, et al. Blood-brain barrier opening with focused ultrasound in Parkinson's disease dementia. *Nat Commun*. 2021;12:779.
10. Hynynen K, McDannold N, Vykhodtseva N, Jolesz FA. Noninvasive MR imaging-guided focal opening of the blood-brain barrier in rabbits. *Radiology*. 2001;220:640–646.
11. Shin J, Kong C, Cho JS, et al. Focused ultrasound-mediated noninvasive blood-brain barrier modulation: preclinical examination of efficacy and safety in various sonication parameters. *Neurosurg Focus*. 2018;44:E15.
12. Xhima K, Markham-Coultes K, Kofoed RH, Saragovi HU, Hynynen K, Aubert I. Ultrasound delivery of a TrkA agonist confers neuroprotection to Alzheimer-associated pathologies. *Brain*. 2021;145:2806–2822.
13. Shin J, Kong C, Lee J, et al. Focused ultrasound-induced blood-brain barrier opening improves adult hippocampal neurogenesis and cognitive function in a cholinergic degeneration dementia rat model. *Alzheimers Res Ther*. 2019;11:110.
14. Mainprize T, Lipsman N, Huang Y, et al. Blood-brain barrier opening in primary brain tumors with non-invasive mr-guided focused ultrasound: a clinical safety and feasibility study. *Sci Rep*. 2019;9:321.
15. Meng Y, Pople CB, Huang Y, et al. Putaminal recombinant glucocerebrosidase delivery with magnetic resonance-guided focused ultrasound in Parkinson's disease: a phase I study. *Mov Disord*. 2022;37:2134–2139.
16. Rezai AR, D'Haese PF, Finomore V, et al. Ultrasound blood–brain barrier opening and aducanumab in Alzheimer's disease. *N Engl J Med*. 2024;390:55–62.
17. Park J, Aryal M, Vykhodtseva N, Zhang YZ, McDannold N. Evaluation of permeability, doxorubicin delivery, and drug retention in a rat brain tumor model after ultrasound-induced blood-tumor barrier disruption. *J Control Release*. 2017;250:77–85.
18. Kofoed RH, Heinen S, Silburt J, et al. Transgene distribution and immune response after ultrasound delivery of rAAV9 and PHP.B to the brain in a mouse model of amyloidosis. *Mol Ther Methods Clin Dev*. 2021;23:390–405.
19. Aslund AKO, Berg S, Hak S, et al. Nanoparticle delivery to the brain—by focused ultrasound and self-assembled nanoparticle-stabilized microbubbles. *J Control Release*. 2015;220:287–294.
20. Rousou C, Schuurmans CCL, Urtti A, et al. Ultrasound and microbubbles for the treatment of ocular diseases: from preclinical research towards clinical application. *Pharmaceutics*. 2021;13:1782.
21. Park J, Zhang Y, Vykhodtseva N, Akula JD, McDannold NJ. Targeted and reversible blood-retinal barrier disruption via focused ultrasound and microbubbles. *PLoS One*. 2012;7:e42754.
22. Touahri Y, Dixit R, Kofoed RH, et al. Focused ultrasound as a novel strategy for noninvasive gene delivery to retinal Muller glia. *Theranostics*. 2020;10:2982–2999.

Downloaded from tvst.arvojournals.org on 11/11/2024

23. Adini I, Ghosh K. Mouse retinal whole mounts and quantification of vasculature protocol. *Bio Protoc*. 2015;5:e1546.
24. Jiang X, Pardue MT, Mori K, et al. Violet light suppresses lens-induced myopia via neuropsin (OPN5) in mice. *Proc Natl Acad Sci USA*. 2021;118:e2018840118.
25. Huang SY, Huang GL. Preparation and drug delivery of dextran-drug complex. *Drug Deliv*. 2019;26:252–261.
26. Wang HF, Huff TB, Zweifel DA, et al. In vitro and in vivo two-photon luminescence imaging of single gold nanorods. *Proc Natl Acad Sci USA*. 2005;102:15752–15756.
27. Kim CS, Li X, Jiang Y, et al. Cellular imaging of endosome entrapped small gold nanoparticles. *MethodsX*. 2015;2:306–315.
28. Lu RW, Li YC, Ye T, et al. Two-photon excited autofluorescence imaging of freshly isolated frog retinas. *Biomed Opt Express*. 2011;2:1494–1503.
29. Wang DS, Hsu FY, Lin CW. Surface plasmon effects on two photon luminescence of gold nanorods. *Opt Express*. 2009;17:11350–11359.
30. Varshosaz J. Dextran conjugates in drug delivery. *Expert Opin Drug Deliv*. 2012;9:509–523.
31. Yang CD, Jessen J, Lin KY. Ultrasound-assisted ocular drug delivery: a review of current evidence. *J Clin Ultrasound*. 2022;50:685–693.
32. Poon C, McMahon D, Hynynen K. Noninvasive and targeted delivery of therapeutics to the brain using focused ultrasound. *Neuropharmacology*. 2017;120:20–37.
33. Kovacs ZI, Kim S, Jikaria N, et al. Disrupting the blood-brain barrier by focused ultrasound induces sterile inflammation. *Proc Natl Acad Sci USA*. 2017;114:E75–E84.
34. Huh H, Park TY, Seo H, et al. A local difference in blood–brain barrier permeability in the caudate putamen and thalamus of a rat brain induced by focused ultrasound. *Sci Rep*. 2020;10:19286.
35. Singh A, Kusunose J, Phipps MA, Wang F, Chen LM, Caskey CF. Guiding and monitoring focused ultrasound mediated blood–brain barrier opening in rats using power Doppler imaging and passive acoustic mapping. *Sci Rep*. 2022;12:14758.

Downloaded from tvst.arvojournals.org on 11/11/2024